A Control Strategy for Efficiency Optimization and Wide ZVS Operation Range in Bidirectional Inductive Power Transfer System

Xiaoming Zhang, Tao Cai, Shanxu Duan, *Senior Member, IEEE,* Hao Feng, Hongsheng Hu, Jintao Niu and Changsong Chen

***Abstract*—The efficiency of bidirectional inductive power transfer (BIPT) systems is strongly dependent on the load. Besides, soft switching operation of power switches is critical to high frequency converter in BIPT systems. In this paper, a triple-phase-shift (TPS) control strategy is proposed to achieve load matching while realizing zero voltage switching (ZVS) for all power switches within entire power range. The load matching condition of bidirectional inductive power transfer system with double-sided LCC compensation network is analyzed. And a dual side phase shift control is proposed to adjust power flow while realizing load matching. To realize ZVS operation, the third phase shift between primary and secondary side is introduced as an extra control variable. A time domain model of double-sided LCC compensation network is established to analyze the ZVS range. With the proposed TPS control, wide ZVS operation range of system can be achieved while maintaining load matching. At last, a scale down prototype of 1kW BIPT system is developed. The experimental results show good agreement with theoretical analysis, all switches realize ZVS within entire power range and a peak efficiency of 94.83% is achieved.**

***Index Terms*—bidirectional inductive power transfer (BIPT), time domain model, triple-phase-shift (TPS) control, zero voltage switching (ZVS)**

I. INTRODUCTION

INDUCTIVE power transfer (IPT) use magnetic coupling to transfer power between two systems without any physical contacts. It is gaining more and more attention due to the advantages of convenience, safety and low maintenance costs. Applications of IPT range from low power systems, such as portable electronic devices [1], [2], biomedical plant [3], [4], to high power systems, such as mining machine, autonomous underwater vehicles [5], [6], electrical vehicles (EVs) [7-11] and trains [12].

Applying IPT to EV for wireless charging is one of the most promising applications, it provides an easy way for charging EVs and extends the driving range, which promotes the popularity of EVs. Currently, studies on wireless charging systems are mainly focused on unidirectional power transfer [13-19], which can only consume power from the grid. A new bidirectional inductive power transfer (BIPT) system is proposed in [20], which has a capacity of two-way power transfer. It extends the IPT to the vehicle-to-grid (V2G) applications, which uses EVs as storage energy and supplies energy back to the grid. Compared with unidirectional inductive power transfer (UIPT) systems, BIPT systems usually feature with higher system order and have more complex control patterns due to the two-way power transfer mode, thereby previous research mainly focuses on the modeling and control of BIPT systems [20-24]. The stationary and dynamic system models of BIPT systems are established in [21] and [22] respectively, which can describe the basic behaviors of BIPT systems and guide the system design. For power flow control, dual side phase shift (DPS) control is considered to be an appropriate approach, which can both regulate the direction and amplitude of power flow [20], [23].

For BIPT systems, system efficiency is highly dependent on the load, which is similar to UIPT systems but more complex because either side can be source or load. To overcome this problem, for UIPT systems, a secondary side active control is necessary, which can convert the equivalent output load impedance to the optimal value dynamically. A most common practice is to cascade a DC/DC converter on the secondary side for load impedance conversion [19, 25, 26]. However, the losses caused by multi-stage converters reduce the overall system efficiency. Besides, the increased system complexity and system cost have to be considered. Using an active rectifier on the secondary side is another choice [27-29]. It realizes load impedance conversion with duty control or phase shift control

Manuscript received March 1, 2018; revised June 12, 2018 and July 27, 2018; accepted September 2, 2018. This work was supported in part by the National Key Research and Development Program of China by MOST (Key technologies of high performance charger for electric vehicles based on advanced power semiconductors, No. 2018YFB0106300) and in part by the Lite-On Power Electronics Technology Research Fund under Grant PRC20161047.

The authors are with the State Key Laboratory of Advanced Electromagnetic Engineering and Technology, School of Electric and Electronic Engineering, Huazhong University of Science and Technology, Wuhan 430074, China (e-mail: xiaomingzhang@hust.edu.cn; caitao@hust.edu.cn; duanshanxu@hust.edu.cn; fhdtc2008@hust.edu.cn; huhongsheng@hust.edu.cn; JT_Niu@hust.edu.cn; ccsfm@163.com).

This article has been accepted for publication in a future issue of this journal, but has not been fully edited. Content may change prior to final publication. Citation information: DOI 10.1109/TIE.2018.2871794, IEEE Transactions on Industrial Electronics

in secondary rectifier. It eliminates the use of a cascaded DC/DC converter so as the losses brought by, and has a higher power density. But the power switches of active rectifier may suffer from hard-switching condition and introduce additional switching losses, which limit the increase of switching frequency. For BIPT systems, which have dual side active structure intrinsically, the secondary full bridge can be readily utilized to perform active impedance conversion. In [30], a dual active bridge phase shift modulation strategy is proposed for efficiency optimization. By properly choosing the phase shift angle of primary and secondary full bridge, the power command and load matching condition can be achieved simultaneously. However, similar to the active rectifier in UIPT systems, it also faces the challenge of hard-switching for both primary and secondary power switches, which constitutes a limitation on the increase of system efficiency. So it is significant to achieve load matching and soft-switching simultaneously for BIPT systems.

To solve the problem， an optimal triple phase shift (TPS) control strategy is proposed for BIPT systems. The paper is structured into five sections: in Section II, load matching condition for high efficiency operation of BIPT systems is analyzed, and an optimal dual side phase shift control is proposed to realize power flow regulation and load matching simultaneously. In Section III, a harmonics based time domain model of BIPT systems is proposed to analyze the ZVS operation range of power switches. Then the third phase shift between primary and secondary full bridges is introduced to achieve ZVS operation over entire power range. In Section IV, a scale down prototype with 1kW output power is presented to validate the proposed time domain model and control strategy. The last section is the conclusion.

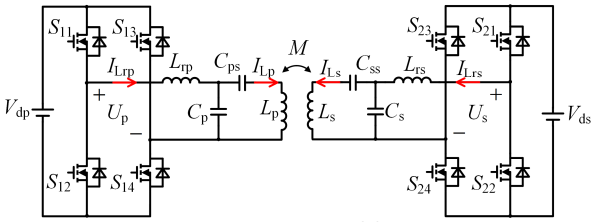

Fig. 1. BIPT system with doubled-sided LCC compensation network

II. Efficiency Analysis of BIPT Systems

In this section, the power transfer profile and efficiency of BIPT systems are analyzed. The load matching concept is introduced to optimize the system efficiency. Due to the advantages of constant coil current, unit power factor and high power transfer capacity, double-sided LCC compensation network is chosen as the resonant network in BIPT systems [31].

A. Power Transfer Profile

The typical BIPT system with double-sided LCC compensation network is shown in Fig. 1. S_{11}-S_{14} and S_{21}-S_{24} are the power switches of primary and secondary side full bridges, respectively. L_p and L_s are the self-inductance of the transmitter and receiver coils. L_{rp}, C_p and C_{ps} are the compensation components of transmitter coil; L_{rs}, C_s and C_{ss} are the compensation components of receiver coil. M is the mutual inductance of the transmitter and receiver coils. V_{dp} is the DC bus voltage of the primary full bridge converter, which is usually provided by the forestage PFC converter and has a constant value. V_{ds} is the secondary DC bus voltage. Since the secondary DC bus is usually connected to the battery via an inductor, V_{ds} is a variable. U_p and U_s are the output voltage of the primary and secondary full bridges, respectively. Considering the primary and secondary side both may work as source or load symmetrically, the system parameters are typically symmetrically designed.

DPS control strategy is employed to control the amplitude and direction of power flow. The driving signals of the power switches and the output voltage of the full bridges are shown in Fig. 2. The upper and lower bridge leg switches on and off complementarily with a duty cycle of 0.5 in constant frequency. S_{13} switches on before S_{11} with a leading phase angle β_p, and S_{23} switches on leading S_{21} with β_s. δ is the phase angle between $U_{p,1}$ and $U_{s,1}$, where $U_{p,1}$ and $U_{s,1}$ are the fundamental output voltage of the primary and secondary full bridges. To realize phase shift between primary and secondary full bridges, the synchronization of primary and secondary side is necessary, which can be achieved by utilizing an auxiliary winding [32]. The dead time between the driving signals is small and has minimal effect on the power transfer characteristics, so it is neglected in the analysis below.

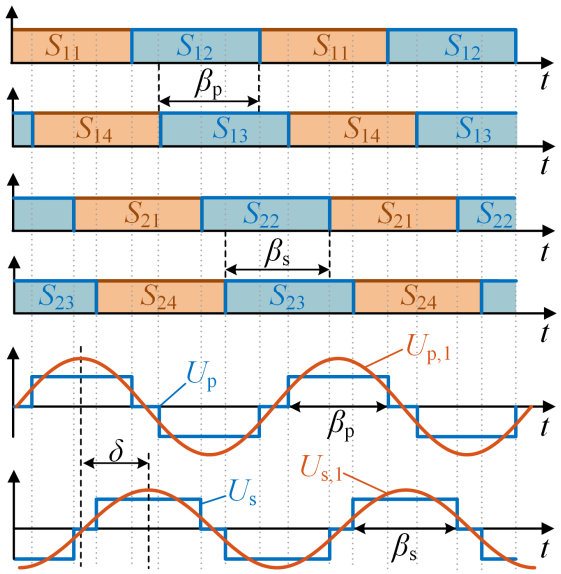

Fig. 2. Dual side phase shift modulation of BIPT system

The transferred power of BIPT system is mainly related to the fundamental component, the high order harmonics have little contribution to the power transfer due to the resonation operation characteristics. To simplify the analysis, the fundamental harmonic approximation (FHA) method is used. The simplified model of BIPT system with FHA method is shown in Fig. 3. R_{Lp} and R_{Ls} are the parasitic resistances of the primary and secondary coils, respectively. R_{Lrp} and R_{Lrs} are the equivalent loss resistances of the compensation inductors branch, which contain the losses of the compensation inductors and the conduction losses of power switches.

The output voltages of the primary and secondary full

This article has been accepted for publication in a future issue of this journal, but has not been fully edited. Content may change prior to final publication. Citation information: DOI 10.1109/TIE.2018.2871794, IEEE Transactions on Industrial Electronics

bridges are replaced by the fundamental component $U_{p,1}$ and $U_{s,1}$, and they can be derived by Fourier series expansion:

$$\dot{U}_{p,1} = \frac{2\sqrt{2}}{\pi} V_{dp} \sin\left(\frac{\beta_p}{2}\right) \tag{1}$$

$$\dot{U}_{s,1} = \frac{2\sqrt{2}}{\pi} V_{ds} \sin\left(\frac{\beta_s}{2}\right) \angle -\delta \tag{2}$$

U_{ps} and U_{sp} are the induced voltages in the primary and secondary coils, respectively, and they are given by

$$\dot{U}_{ps} = j\omega M \dot{I}_{Ls} \tag{3}$$

$$\dot{U}_{sp} = j\omega M \dot{I}_{Lp} \tag{4}$$

where M is the mutual inductance between transmitter and receiver coils. M can be expressed as a function of coupling coefficient k between transmitter and receiver coils

$$M = k\sqrt{L_p L_s} \tag{5}$$

Assuming the system parameters are symmetrical, the system frequency is ω, the characteristics impedance of the system is denoted as

$$X = \omega L_{rp} = \frac{1}{\omega C_p} = \omega L_{rs} = \frac{1}{\omega C_s} \tag{6}$$

The ratio of both primary and secondary coil's inductance and that of the respective compensation inductor is defined as

$$\alpha = \frac{L_p}{L_{rp}} = \frac{L_s}{L_{rs}} \tag{7}$$

α is large than 1 to boost the power transfer capacity of the double-sided LCC compensation network.

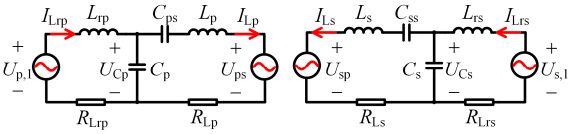

Fig. 3. Simplified FHA model of BIPT systems

The series compensation capacitors are chosen to make sure the primary and secondary coils are fully compensated [31]

$$C_{ps} = \frac{1}{\omega^2 \left(L_p - L_{rp}\right)} \tag{8}$$

$$C_{ss} = \frac{1}{\omega^2 \left(L_s - L_{rs}\right)} \tag{9}$$

Neglecting the loss resistances and using the Kirchhoff's voltage law, the transferred active power and reactive power are calculated by

$$P = \mathrm{Re}\left\{-\dot{U}_{s,1}\dot{I}^*_{Lrs}\right\} = \frac{\alpha k}{X} U_{p,1} U_{s,1} \sin(\delta) \tag{10}$$

$$Q = \mathrm{Im}\left\{-\dot{U}_{s,1}\dot{I}^*_{Lrs}\right\} = -j\frac{\alpha k}{X} U_{p,1} U_{s,1} \cos(\delta) \tag{11}$$

From (10), the power transfer direction is decided by phase angle δ. When $0<\delta<\pi$, power is transferred from primary side to secondary side, when $-\pi<\delta<0$, power flow is reversed. The maximum power transfer is achieved when δ is $\pi/2$ or $-\pi/2$, where the reactive power is minimized simultaneously. So it is preferred to work in $\delta=\pm\pi/2$ to reduce the VA requirement of the power supply and to get a higher efficiency. The amplitude of the active power is also related to the fundamental voltages of the full bridges in the primary and secondary side, which can be regulated by the phase shift angle β_p and β_s.

B. Efficiency Analysis

The circuit losses of BIPT system mainly include the coils losses, compensation inductors losses, and the conduction and switching losses of power switches. The switching losses are neglected in this section, the other losses are modeled with R_{Lp}, R_{Ls}, R_{Lrp} and R_{Lrs} as shown in Fig. 3. Assuming $R_{Lp}=R_{Ls}$ and $R_{Lrp}=R_{Lrs}$ due to the symmetrical system parameters, the overall losses are given by

$$\begin{aligned} P_{loss} &= I_{Lrp}^2 R_{Lrp} + I_{Lp}^2 R_{Lp} + I_{Lrs}^2 R_{Lrs} + I_{Ls}^2 R_{Ls} \\ &= \frac{\alpha^2 k^2 \left(U_{p,1}^2 + U_{s,1}^2\right)}{X^2} R_r + \frac{U_p^2 + U_s^2}{X^2} R \end{aligned} \tag{12}$$

where coil resistance $R_{Lp}=R_{Ls}=R$, equivalent inductor resistance $R_{Lrp}=R_{Lrs}=R_r$.

Then the system efficiency is calculated approximately by

$$\eta \approx \frac{|P|}{|P| + P_{loss}} \tag{13}$$

Substituting (12) into (13), the power transfer efficiency can be derived as

$$\eta \approx \frac{\alpha k X |\sin\delta|}{\alpha k X |\sin\delta| + \left(\alpha^2 k^2 R_r + R\right) T + \left(\alpha^2 k^2 R_r + R\right) \frac{1}{T}} \tag{14}$$

where T is the ratio of the excitation voltages in primary and secondary side

$$T = \frac{U_{s,1}}{U_{p,1}} \tag{15}$$

The system efficiency against the excitation voltage ratio T under different phase angle δ is shown in Fig. 4. It is obvious the system efficiency varies with the excitation voltage ratio. And under a certain excitation voltage ratio, the maximum system efficiency is achieved. The phase angle δ has an impact on the system efficiency. The maximum system efficiency is achieved when $\delta=\pm90°$. When δ slightly deviates around $\pm90°$, system efficiency reduces mildly, and only with a large deviation, the efficiency reduction is distinct.

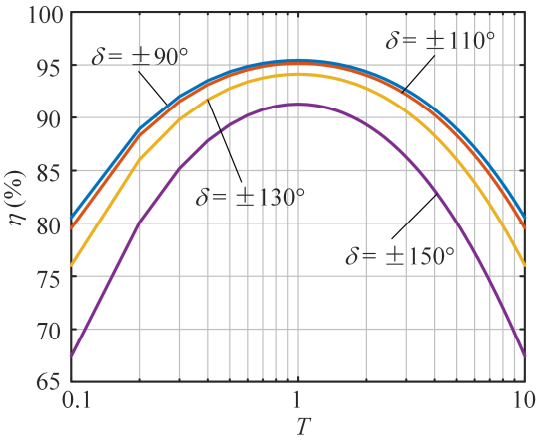

Fig. 4. Power transfer efficiency against excitation voltage ratio T

This article has been accepted for publication in a future issue of this journal, but has not been fully edited. Content may change prior to final publication. Citation information: DOI 10.1109/TIE.2018.2871794, IEEE Transactions on Industrial Electronics

Solving the derivative of η with respect to T, the excitation voltage ratio to get the maximum system efficiency is derived as

$$\frac{d\eta}{dT}=0\Rightarrow T=1 \tag{16}$$

From (16), it is obvious that in order to get maximum system efficiency, equal primary and secondary excitation voltages should be implemented. It should be noted that the same matching condition is held for different phase shift angle δ.

The equivalent AC load resistance under T=1 is calculated as

$$R_{opt}=\frac{U_{s,1}^2}{P}=\left(\alpha k\sin\delta\right)^{-1}X \tag{17}$$

From (17), the equivalent AC load resistance is a constant and unrelated to output power under the optimal excitation voltage ratio. It means that for different output power, with an optimal equivalent AC load resistance, the system efficiency can be maximized. So the matching of primary and secondary side excitation voltages in BIPT system is equal to the load matching concept in UIPT systems.

With excitation voltage matched, the maximum system efficiency is calculated as

$$\eta_{\max}=\frac{\alpha kX\left|\sin\delta\right|}{\alpha kX\left|\sin\delta\right|+2\left(\alpha^2k^2R_r+R\right)}=\frac{\left|\sin\delta\right|}{\left|\sin\delta\right|+2\left(\dfrac{\alpha k}{Q_r}+\dfrac{1}{kQ}\right)} \tag{18}$$

where, Q_r and Q are the quality factor of the compensated inductors and the coils, respectively, which are defined as

$$Q_r=\frac{\omega L_{rp}}{R_{Lrp}}=\frac{\omega L_{rs}}{R_{Lrs}} \tag{19}$$

$$Q=\frac{\omega L_p}{R_{Lp}}=\frac{\omega L_s}{R_{Ls}} \tag{20}$$

C. Control Strategy for Load Matching

For maximum power transfer and high system efficiency, phase shift angle δ is set to ±90° traditionally. Here, the phase shift angle β_p and β_s are used to realize load matching, namely voltage matching of the excitation voltages in BIPT systems.

Substituting (1) and (2) into (16) yields

$$\frac{\sin\left(\beta_p/2\right)}{\sin\left(\beta_s/2\right)}=T_{dc}=\frac{V_{ds}}{V_{dp}} \tag{21}$$

where, T_{dc} is the voltage ratio of primary and secondary DC bus. From (21), β_p and β_s are a function of T_{dc}. β_p and β_s can be controlled with respect to T_{dc}, so as to achieve load matching. For a given output power P, the optimal β_p and β_s can be calculated as

$$\beta_p=2\sin^{-1}\left(\frac{\pi}{2V_{dp}}\sqrt{\frac{X}{2\alpha k}P}\right) \tag{22}$$

$$\beta_s=2\sin^{-1}\left(\frac{\pi}{2V_{ds}}\sqrt{\frac{X}{2\alpha k}P}\right) \tag{23}$$

The optimal β_p and β_s are monotonous about output power and only related to one side DC bus voltage, which makes a simple control possible. The relationship between β_p and β_s under load matching are shown in Fig. 5. When T_{dc}<1, with an increase of output power, β_p and β_s increase monotonously according to (21). In heavy load, β_p and β_s cannot satisfied (21) anymore due to the unmatched DC bus voltages, so β_s is kept 180° to approximate unit excitation voltage ratio and maintain high efficiency. The similar situation occurs when T_{dc}>1, and β_p is maintained 180° to achieve high efficiency. Only when T_{dc}=1, (21) can be satisfied over entire power range.

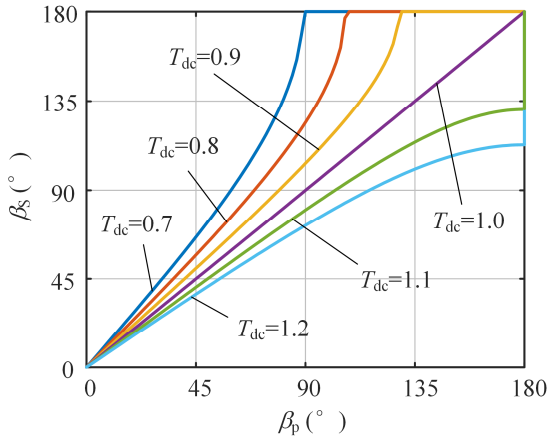

Fig. 5. Relationship between β_p and β_s under load matching

III. Soft-Switching Realizing with Load Matching

In the previous section, load matching of BIPT systems is achieved by DPS control strategy. However, with only DPS control, the ZVS operation range of system is narrow, the power switches may suffer hard-switching, which cause large switching losses. In this section, an optimal TPS control strategy is introduced. The phase shift angle δ is not set to ±90°, whereas it is used as an additional control variable to produce a lagging current for soft-switching realization. To determine the ZVS range of power switches, a harmonic based time domain system model is established, and then the TPS control strategy is analyzed.

A. Time Domain Model

To determine the ZVS range of BIPT systems, the output currents of full bridges should be calculated and the time domain analysis should be employed. Although FHA model is accurate enough for power calculating, it has a non-negligible error in determining ZVS range due to the high order harmonics in output currents of full bridges. To take the harmonics into consideration, the squared ware excitation voltages are implemented as shown in Fig. 6. The loss resistances are neglected in the model.

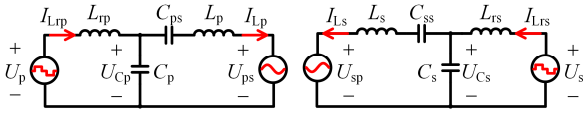

Fig. 6. Circuit model of BIPT systems considering high order harmonics

Due to the symmetry of system parameters, forward and reversed power transfer characteristics are similar, so only the forward power transfer mode is analyzed below. Assuming power is transferred from primary side to secondary side, the lagging phase shift angle π/2, corresponding to the maximum

power transfer point, is chosen as the basic phase shift angle. And a phase shift compensated angle $\Delta\delta$ is taken into consideration, which yields

$$\delta = \pi/2 + \Delta\delta \tag{24}$$

where, phase shift compensated angle $\Delta\delta$ is ranged from -π/2 to π/2.

The circuit model is with high order and hard to get an analytic expression. Due to the filtering function of L_{rp}, C_p, L_{rs} and C_s, there are rarely high order harmonics in the coil current. So the coil current can be calculated by FHA model instead of precise model for simplification.

The steady state waveforms of coil currents calculated by FHA method are

$$I_{Lp}(t) = \frac{4}{\pi}\frac{V_{dp}}{X}\sin\frac{\beta_p}{2}\sin\left(\omega t - \frac{\pi}{2}\right) \tag{25}$$

$$I_{Ls}(t) = -\frac{4}{\pi}\frac{V_{ds}}{X}\sin\frac{\beta_s}{2}\sin(\omega t - \Delta\delta) \tag{26}$$

U_{ps} and U_{sp} are induced by I_{Ls} and I_{Lp} respectively, so they can also be calculated by FHA method. Then the voltage across C_p which equal to the sum of U_{ps} and voltage across L_p and C_{ps} is derived as

$$\begin{aligned}\dot{U}_{Cp} &= \dot{U}_{ps} + \dot{I}_{Lp}\times\left(j\omega L_p + 1/j\omega C_{ps}\right)\\ &= \frac{2\sqrt{2}}{\pi}\alpha k V_{ds}\sin\frac{\beta_s}{2}\angle -\left(\frac{\pi}{2}+\Delta\delta\right) + \frac{2\sqrt{2}}{\pi}V_{dp}\sin\frac{\beta_p}{2}\end{aligned} \tag{27}$$

The time domain expression of U_{Cp} is

$$U_{Cp}(t) = \frac{4}{\pi}V_{dp}\sin\frac{\beta_p}{2}\sin(\omega t) - \frac{4}{\pi}\alpha k V_{ds}\sin\left(\frac{\beta_s}{2}\right)\cos(\omega t - \Delta\delta) \tag{28}$$

Similarly, the time domain expression of U_{Cs} is derived as

$$U_{Cs}(t) = -\frac{4}{\pi}V_{ds}\sin\frac{\beta_s}{2}\cos(\omega t - \Delta\delta) + \frac{4}{\pi}\alpha k V_{dp}\sin\frac{\beta_p}{2}\sin(\omega t) \tag{29}$$

According to (28) and (29), the voltage of C_p and C_s are sinusoidal, too. So the sinusoidal voltage sources can be implemented to simplify the circuit further as shown in Fig. 7.

As shown in Fig. 7, part of the circuit model are replaced by voltage sources, so the system order is reduced, which make it easy for calculation. The circuit mode can be described with only two differential equations:

$$U_p(t) - U_{Cp}(t) = L_{rp}\frac{dI_{Lrp}(t)}{dt} \tag{30}$$

$$U_s(t) - U_{Cs}(t) = L_{rs}\frac{dI_{Lrs}(t)}{dt} \tag{31}$$

By integrating (30) and (31), the expression of the primary and secondary full bridge output current can be derived. Fig. 8 shows the key waveforms of the simplified circuit model. t_0 is the zero crossing point of the primary fundamental voltage. t'_0 is chosen as the beginning for calculating secondary side waveforms and has a value of $\Delta\delta/\omega$. Due to the symmetry, just the first half switching period will be analyzed, and the sub states in the second half period can be analyzed similarly. By solving the differential equations, the output current of primary side is expressed in (35), shown at the bottom of the page. Similarly, the output current of secondary side is solved as (36), shown at the bottom of the page.

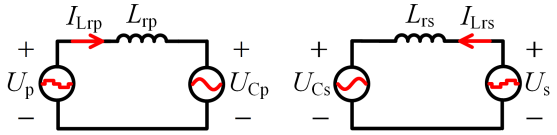

Fig. 7. Simplified circuit model of BIPT systems considering high order harmonics

Due to the symmetry of the current waveforms, it is obvious

$$I_{Lrp}(t_3 = \pi/\omega) = -I_{Lrp}(t_0 = 0) \tag{32}$$

So the primary output current in t_0 is calculated as

$$I_{Lrp}(t_0) = \frac{4V_{dp}}{\pi X}\sin\frac{\beta_p}{2} - \frac{V_{dp}}{X}\frac{\beta_p}{2} - \frac{4\alpha k V_{ds}}{\pi X}\sin\frac{\beta_s}{2}\sin(\Delta\delta) \tag{33}$$

Similarly, the secondary output current in t'_0 is derived as

$$I_{Lrs}(t'_0) = \frac{4\alpha k V_{dp}}{\pi X}\sin\frac{\beta_p}{2}\cos(\Delta\delta) \tag{34}$$

B. Soft-Switching Realization

By the time domain model proposed previous section, primary output current in switching points t_1 and t_2 are calculated as

$$I_{Lrp}(t) = \begin{cases} I_{Lrp}(t_0) + \frac{4V_{dp}}{\pi X}\sin\frac{\beta_p}{2}\left[\cos(\omega t) - 1\right] + \frac{4\alpha k V_{ds}}{\pi X}\sin\frac{\beta_s}{2}\left[\sin(\omega t - \Delta\delta) + \sin(\Delta\delta)\right], & t_0 < t < t_1 \\ I_{Lrp}(t_1) + \frac{V_{dp}}{X}\left(\omega t - \frac{\pi - \beta_p}{2}\right) + \frac{4V_{dp}}{\pi X}\sin\frac{\beta_p}{2}\left[\cos(\omega t) - \sin\frac{\beta_p}{2}\right] + \frac{4\alpha k V_{ds}}{\pi X}\sin\frac{\beta_s}{2}\left[\sin(\omega t - \Delta\delta) - \cos\left(\frac{\beta_p}{2} + \Delta\delta\right)\right], & t_1 < t < t_2 \\ I_{Lrp}(t_2) + \frac{4V_{dp}}{\pi X}\sin\frac{\beta_p}{2}\left[\cos(\omega t) + \sin\frac{\beta_p}{2}\right] + \frac{4\alpha k V_{ds}}{\pi X}\sin\frac{\beta_s}{2}\left[\sin(\omega t - \Delta\delta) - \cos\left(\frac{\beta_p}{2} - \Delta\delta\right)\right], & t_2 < t < t_3 \end{cases} \tag{35}$$

$$I_{Lrs}(t) = \begin{cases} I_{Lrs}(t'_0) - \frac{V_{ds}}{X}(\omega t - \Delta\delta) + \frac{4V_{ds}}{\pi X}\sin\frac{\beta_s}{2}\sin(\omega t - \Delta\delta) + \frac{4\alpha k V_{dp}}{\pi X}\sin\frac{\beta_p}{2}\left[\cos(\omega t) - \cos(\Delta\delta)\right], & t'_0 < t < t_7 \\ I_{Lrs}(t_6) + \frac{4V_{ds}}{\pi X}\sin\frac{\beta_s}{2}\left[\sin(\omega t - \Delta\delta) - \sin\frac{\beta_s}{2}\right] + \frac{4\alpha k V_{dp}}{\pi X}\sin\frac{\beta_p}{2}\left[\cos(\omega t) - \cos\left(\frac{\beta_s}{2} + \Delta\delta\right)\right], & t_7 < t < t_8 \\ I_{Lrs}(t_7) + \frac{V_{ds}}{X}\left(\omega t - \frac{2\pi - \beta_s}{2} - \Delta\delta\right) + \frac{4V_{ds}}{\pi X}\sin\frac{\beta_s}{2}\left[\sin(\omega t - \Delta\delta) - \sin\frac{\beta_s}{2}\right] + \frac{4\alpha k V_{dp}}{\pi X}\sin\frac{\beta_p}{2}\left[\cos(\omega t) + \cos\left(\frac{\beta_s}{2} - \Delta\delta\right)\right], & t_8 < t < t_9 \end{cases} \tag{36}$$

This article has been accepted for publication in a future issue of this journal, but has not been fully edited. Content may change prior to final publication. Citation information: DOI 10.1109/TIE.2018.2871794, IEEE Transactions on Industrial Electronics

$$I_{Lrp}(t_1)=-\frac{V_{dp}}{X}\frac{\beta_p}{2}+\frac{4V_{dp}}{\pi X}\sin^2\frac{\beta_p}{2}+\frac{4\alpha k V_{ds}}{\pi X}\sin\frac{\beta_s}{2}\cos\left(\frac{\beta_p}{2}+\Delta\delta\right) \quad (37)$$

$$I_{Lrp}(t_2)=\frac{V_{dp}}{X}\frac{\beta_p}{2}-\frac{4V_{dp}}{\pi X}\sin^2\frac{\beta_p}{2}+\frac{4\alpha k V_{ds}}{\pi X}\sin\frac{\beta_s}{2}\cos\left(\frac{\beta_p}{2}-\Delta\delta\right) \quad (38)$$

Similarly, the secondary output current in switching points t_7 and t_8 are calculated as

$$I_{Lrs}(t_7)=-\frac{V_{ds}}{X}\frac{\beta_s}{2}+\frac{4V_{ds}}{\pi X}\sin^2\frac{\beta_s}{2}+\frac{4\alpha k V_{dp}}{\pi X}\sin\frac{\beta_p}{2}\cos\left(\frac{\beta_s}{2}+\Delta\delta\right) \quad (39)$$

$$I_{Lrs}(t_8)=-\frac{V_{ds}}{X}\frac{\beta_s}{2}+\frac{4V_{ds}}{\pi X}\sin^2\frac{\beta_s}{2}-\frac{4\alpha k V_{dp}}{\pi X}\sin\frac{\beta_p}{2}\cos\left(\frac{\beta_s}{2}-\Delta\delta\right) \quad (40)$$

ZVS is obtained by ensuring that power switches turn on with drain-source voltage clamped to zero by conducting the antiparallel diode. To ensure ZVS for both side power switches, the following constraints should be satisfied:

$$I_{Lrp}(t_1)<0, I_{Lrp}(t_2)>0, I_{Lrp}(t_4)>0, I_{Lrp}(t_5)<0, \quad I_{Lrs}(t_7)<0, I_{Lrs}(t_8)<0, I_{Lrs}(t_{10})>0, I_{Lrs}(t_{11})>0 \quad (41)$$

Due to the symmetry of current waveforms, only the constraints of t_1, t_2, t_7 and t_8 need to be satisfied. Besides, since $0<\beta_p<\pi$, $0<\beta_s<\pi$, $-\pi/2<\Delta\delta<\pi/2$, it is easy to get

$$I_{Lrp}(t_1)+I_{Lrp}(t_2)=\frac{8V_{ds}}{\pi X}\cos\frac{\beta_p}{2}\sin\frac{\beta_s}{2}\cos(\Delta\delta)>0 \quad (42)$$

It can be seen from (42) that if $I_{Lrp}(t_1)<0$, $I_{Lrp}(t_2)>0$ must be satisfied. So to obtain ZVS for all primary side switches, it only needs to satisfy $I_{Lrp}(t_1)<0$. Similarly, for ZVS of all secondary side switches, only $I_{Lrs}(t_7)<0$ need to be satisfied. In a word, the necessary constraints to achieve ZVS of all power switches in both primary and secondary side are

$$I_{Lrp}(t_1)<0, I_{Lrs}(t_7)<0 \quad (43)$$

The ZVS operation range for primary and secondary side switches with $\Delta\delta=0$ under a DC bus ratio of 0.8 is shown in Fig. 9. The red dashed line is the locus of β_p and β_s with load matching control strategy proposed the last section. It is obvious the system has a narrow ZVS range, only with small β_p and β_s or with large β_p and β_s, namely in heavy load or light load, ZVS of both side switches can be obtained. In half load, both side switches suffer from hard-switching condition.

From (11), if $U_{s,1}$ lagging $U_{p,1}$ more than 90°, namely $\Delta\delta>0$, a positive active power is produced, which means an inductive impedance is inserted in circuit and an inductive current is generated. A resonant converter with an inductive impedance is easier to realize ZVS. A slight shift of δ around $\pm 90°$ has little influence on system efficiency as shown in Fig. 4, which means a small $\Delta\delta$ can be adopted to realize ZVS without significantly affecting the system efficiency.

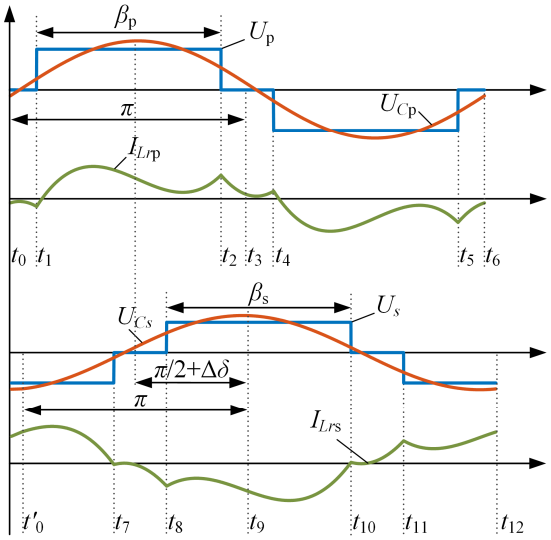

Fig. 8. Key waveforms of double-sided LCC compensation network

The ZVS operation range with different $\Delta\delta$ under a DC bus ratio of 0.8 is shown in Fig. 10. As can be seen, with the increment of $\Delta\delta$, the ZVS range is enlarged too. When $\Delta\delta=30°$, the whole red dashed line is within the yellow zone, which means ZVS within entire power range can be realized.

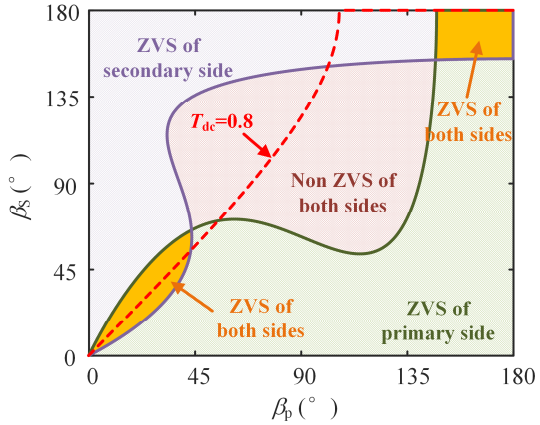

Fig. 9. ZVS range of primary and secondary side switches with $\Delta\delta=0$

Adopting a large $\Delta\delta$ is able to realize ZVS within entire power range, however a large $\Delta\delta$ increase the reactive power of system and increase the requirement of VA rate of supply source. A large $\Delta\delta$ also bring a large switching current, which increases the turn-off losses. Besides, in light and heavy duty, ZVS can be obtained only with $\delta=\pm 90°$ and without a compensation angle $\Delta\delta$. So it is no need to compensate δ within entire power range, only an appropriate compensation angle $\Delta\delta$ need to be applied in half duty.

By solving $I_{Lrp}(t_1)=0$ and $I_{Lrs}(t_7)=0$, the minimal $\Delta\delta$ to realize ZVS while maintaining a minimal reactive power in entire power range can be got. But actually, there is a parallel parasitic capacitor between source drain in physical power switches. To realize ZVS, the output current of full bridges in dead time need large enough to discharge the voltage of the parallel capacitor

This article has been accepted for publication in a future issue of this journal, but has not been fully edited. Content may change prior to final publication. Citation information: DOI 10.1109/TIE.2018.2871794, IEEE Transactions on Industrial Electronics

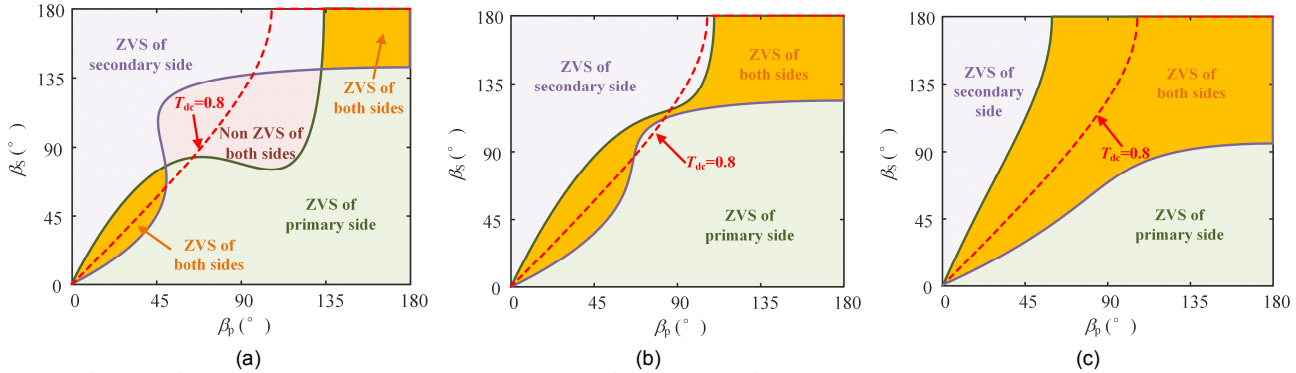

Fig. 10. ZVS range of primary and secondary side switches under DC bus voltage of 0.8 with (a) Δδ=10°, (b) Δδ=20° and (c) Δδ=30°

to zero before conducting the antiparallel diode. The required discharging current can be calculated by the parallel capacitor. With the discharging current I_{dead}, the critical compensation phase angle for ZVS realization of primary and secondary power switches respectively can be derived as

$$\Delta\delta_1 = -\frac{\beta_p}{2} + \cos^{-1}\left(\frac{2\pi XI_{dead} + V_{dp}\left(\beta_p\pi - 8\sin^2\left(\beta_p/2\right)\right)}{8\alpha k V_{ds}\sin\left(\beta_s/2\right)}\right) \quad (44)$$

$$\Delta\delta_2 = -\frac{\beta_s}{2} + \cos^{-1}\left(\frac{2\pi XI_{dead} + V_{ds}\left(\beta_s\pi - 8\sin^2\left(\beta_s/2\right)\right)}{8\alpha k V_{dp}\sin\left(\beta_p/2\right)}\right) \quad (45)$$

The critical compensation phase angle may be minus, which means ZVS can realize even without a compensation. So the optimal compensation phase angle for ZVS realization of all power switches in both primary and secondary side while having a minimal reactive power can be derived as

$$\Delta\delta_{opt} = \max\left(\Delta\delta_1, \Delta\delta_2, 0\right) \quad (46)$$

The optimal compensation phase angle $\Delta\delta$ under different coupling coefficient k is shown in Fig. 11, ideal case without considering the parallel parasitic capacitor of switches and different I_{dead} which considering the parallel parasitic capacitor are discussed. As can be seen, the compensation phase angle $\Delta\delta$ changes with output power and different k. For ideal case, no compensation or little compensation is need under heavy duty and light duty, however a larger $\Delta\delta$ is need under middle duty. When considering the parasitic capacitor, the necessary $\Delta\delta$ increases over entire power range, especially light duty. This is because the full bridge output current is small in light duty, so a larger $\Delta\delta$ is needed to produce enough current for discharging the parasitic capacitor. Considering different coupling coefficient k, the necessary compensation angle is smaller for a smaller k under a certain output power under ideal case. This is because for a certain output power, when work under a smaller k, the phase shift angle of full bridges is larger, which is easier to realize ZVS, so a smaller $\Delta\delta$ is needed. When parasitic capacitor is considered, the conclusion is similar, but in light duty may have roughly equal $\Delta\delta$. It can be seen from Fig. 11, for a wide coupling coefficient operation range, ZVS realization for all power switches within entire power range still can be achieved.

For a reversed power flow, the phase shift angle between primary and secondary fundamental excitation voltages is defined as -π/2-Δδ, and the same conclusion still holds.

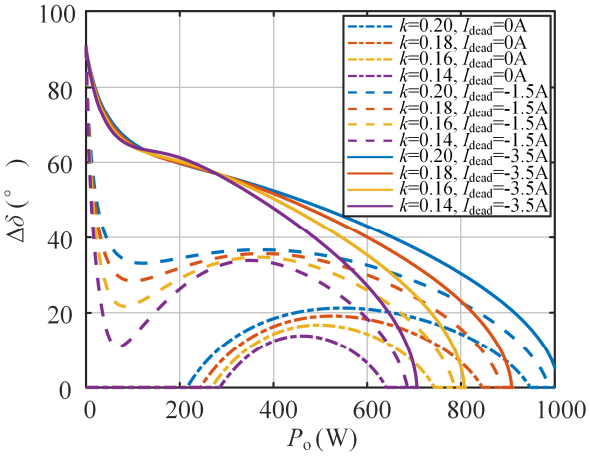

Fig. 11. Compensation phase shift angle Δδ within entire power range under different coupling coefficient k

IV. Experimental Verification

For experimental validation, a scale down BIPT system of 1kW was built, as shown in Fig. 12. The system specifications are given in Table I. The coil and compensation component parameters of primary and secondary side are symmetrically designed. The primary side DC bus voltage is 200V, secondary side DC bus voltage is varied from 160V to 240V. Considering a maximal misalignment of ±100mm with the designed coils, the coupling coefficient k is between 0.14 and 0.2. Infineon high speed power MOSFET IPW65R041CFD was chosen as the switches of both sides. The power MOSFETs were intended for higher power experiments in our future work and was not very suitable for low power and low voltage experiments. Due to the large output capacitance of the MOSFETs in low voltage, current for ZVS realization in switching point is as large as -3.5A. A dead time of 353ns was set to avoid shoot-through of bridge legs and ZVS realization of both side bridges.

To verify the effectiveness of the proposed time domain model, open loop test is carried out. The output voltage and current waveforms of primary and secondary side bridge with a transferred power of 237W and T_{dc}=0.8 are shown in Fig. 13. As can be seen, the experimental current waveforms are in good agreement with the proposed time domain model waveforms for both primary and secondary sides. The time domain model is accurate enough to analyze the ZVS range of system. Only

This article has been accepted for publication in a future issue of this journal, but has not been fully edited. Content may change prior to final publication. Citation information: DOI 10.1109/TIE.2018.2871794, IEEE Transactions on Industrial Electronics

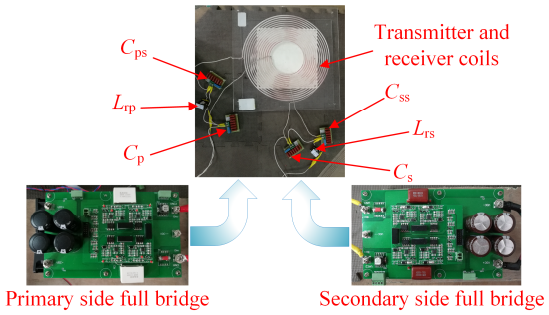

Fig. 12. Photograph of the BIPT system prototype

TABLE I
SPECIFICATIONS OF THE PROPOSED BIPT SYSTEM FOR EXPERIMENTS

Symbol	Parameters	Value	Unit
V_{dp}	Primary side DC bus voltage	200	V
V_{ds}	Secondary side DC bus voltage	160-240	V
f	Switching frequency	85	kHz
k	Coupling coefficient	0.14-0.2	
L_p	Transmitter coil inductance	48.4	μH
R_{Lp}	Transmitter coil ESR	57	mΩ
C_{ps}	Primary series compensation capacitor	146.5	nF
C_p	Primary parallel compensation capacitor	146.5	nF
L_{rp}	Primary compensation inductance	24.3	μH
L_s	Receiver coil inductance	47.5	μH
R_{Ls}	Receiver coil ESR	58	mΩ
C_{ss}	Secondary series compensation capacitor	146.8	nF
C_s	Secondary parallel compensation capacitor	145.9	nF
L_{rs}	Secondary compensation inductance	24.3	μH

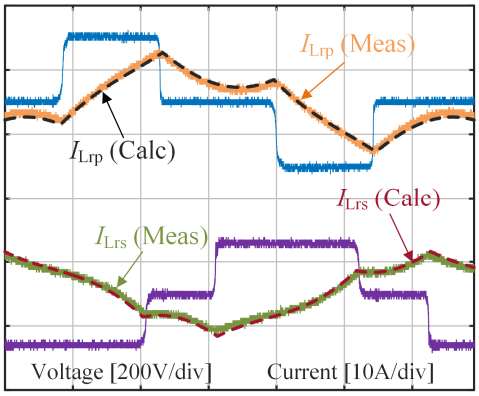

Fig. 13. Output voltage and current waveforms of primary and secondary side bridge under T_{dc}=0.8

little error exists, which is mainly due to the dead time and slight deviation of system parameters.

With only DPS control for load matching, and δ is set to constant $\pm 90°$, the experimental output voltage and current of primary and secondary full bridge in half duty for k=0.2 and T_{dc}=1.0 are shown in Fig. 14. As can be seen, with DPS control, only half of the MOSFETs can realize ZVS, the other half work in hard switching. This cause a lot of losses and voltage spike on MOSFETs, which may damage the MOSFETs. The phase shift angle of primary and secondary full bridge are controlled to have equal excitation voltages for both side, however it can be seen the secondary side duty cycle is larger. The error is mainly caused by the dead time, due to the positive current in switching point P_1, primary full bridge output voltage during dead time is zero, which cause a duty cycle loss. Similarly, a duty cycle loss occurs in switching point P_2. The duty cycle error is equal to two times the dead time, and may be concerned for non-negligible dead time in small duty cycle.

With the proposed TPS control strategy, experimental output current and voltage waveforms at 1/4 load, half load and full load for k=0.2 and T_{dc}=1.0 are provided in Fig. 15. As can be see, all MOSFETs of primary and secondary realize ZVS over the wide power range. The output currents of primary and secondary side full bridge in switching point are negative and close to the target value -3.5A with a max error of 0.4A. The compensation angle $\Delta\delta$ at 1/4 load is as large as 57.5°. This is because in light duty, the output current is small, whereas the output capacitor of MOSFETs is large. So a large compensation angle is needed to produce a large inductive current for fully discharging the output capacitor of MOSFETs. The duty cycle error is smaller in ZVS operation, the minor error is mainly due to the charging and discharging of the output capacitor of MOSFETs during dead time and the difference of drive signals.

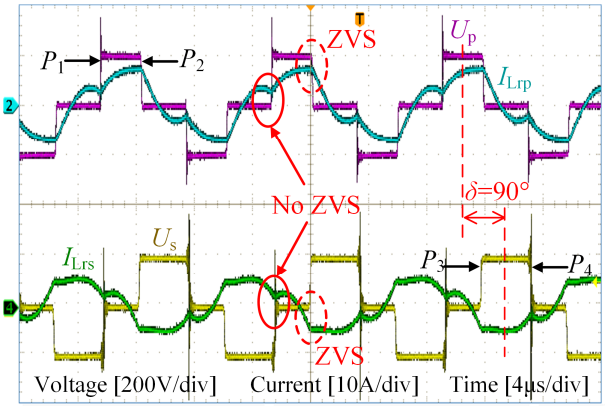

Fig. 14. Output voltage and current waveforms of primary and secondary full bridge with dual side phase shift control in half duty for k=0.2 and T_{dc}=1.0

The ZVS operation of system under a maximal misalignment is tested, too. The experimental waveforms at different load are shown in Fig. 16. Both primary and secondary side MOSFETs realize ZVS for k=0.14 within the wide output power range. The minimal switching current is close to the desired value -3.5A too. So with the proposed TPS control, ZVS operation of both side MOSFETs are achieved for wide power range and coupling coefficient.

When the transmitter and receiver coils are aligned, the overall system efficiency of the prototype with DC bus voltage ratio of 0.8, 1.0 and 1.2 under DPS control and TPS control are given in Fig. 17. The system has poor efficiency in light duty and middle duty for different DC bus ratio when only DPS control is applied, this is because of the hard switching of the primary and secondary MOSFETs. When the third phase shift is adopted for TPS control, the system achieves ZVS for all switches. The switching losses is eliminated, and the system efficiency in light duty and middle duty is increased to more than 90%. Load matching is realized for T_{dc}=1 in all power range, and the highest system efficiency is 94.83% at 1021W. Due to the mismatching of primary and secondary side DC bus voltages when T_{dc}=0.8 and 1.2, equal excitation voltages cannot be applied in heavy duty. The phase shift angle of full bridge in lower DC bus voltage side is kept to π in heavy duty for high system efficiency, and highest efficiency of 94.8% and 94.06%

This article has been accepted for publication in a future issue of this journal, but has not been fully edited. Content may change prior to final publication. Citation information: DOI 10.1109/TIE.2018.2871794, IEEE Transactions on Industrial Electronics

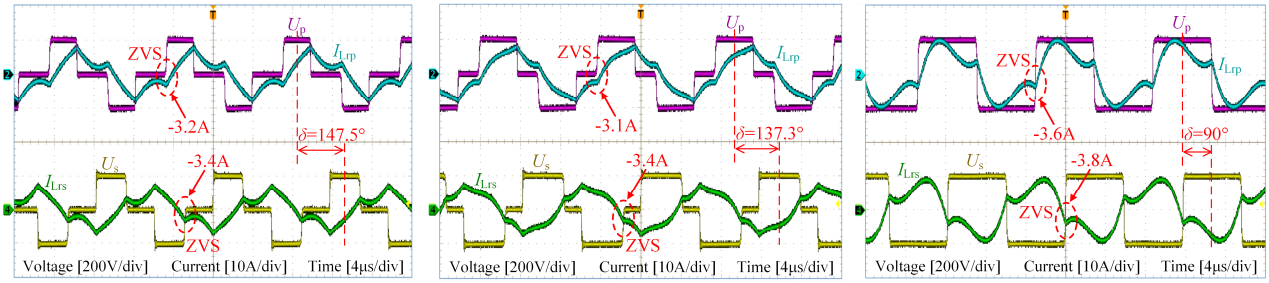

(a) (b) (c)

Fig. 15. Output voltage and current waveforms of primary and secondary side bridge for k=0.2 and T_{dc}=1 at (a) 1/4 load, (b) half load, (c) full load

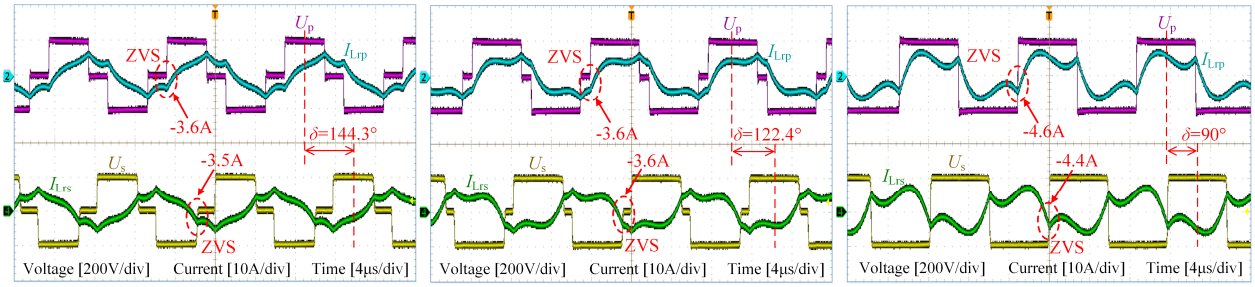

(a) (b) (c)

Fig. 16. Output voltage and current waveforms of primary and secondary side bridge for k=0.14 and T_{dc}=1 at (a) 1/4 load, (b) half load, (c) maximal load*

* The output power in k=0.14 cannot reach 1kW, the measured maximal output power in k=0.14 is 682W.

is still achieved for T_{dc}=0.8 and T_{dc}=1.2 respectively. The system efficiency dropped in light duty is mainly due to the large compensated angle $\Delta\delta$. When output power is 159W for T_{dc}=0.8, $\Delta\delta$ is as large as 63.5°, which may seriously damage the system efficiency. Compared with the large losses caused by hard switching, the reactive losses brought by large $\Delta\delta$ is still relatively small and is worth it. The system efficiency can be further improved by using a more appropriate MOSFET with a smaller output capacitor in low power and low voltage.

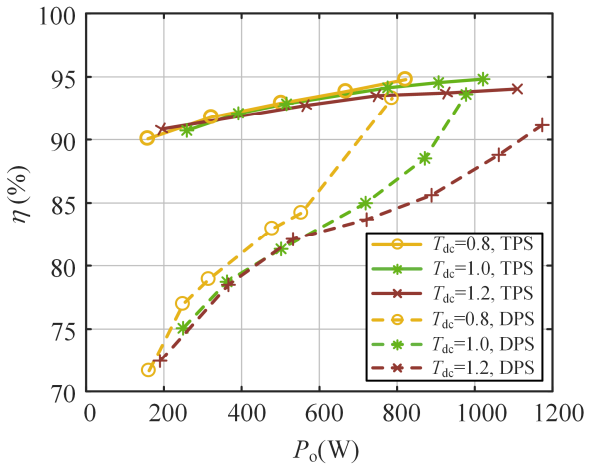

Fig. 17. Overall system efficiency against output power for different DC bus voltage ratio under DPS and TPS control

V. Conclusion

In this paper, a control strategy for efficiency optimization and wide ZVS operation range in BIPT systems is proposed. The load matching condition for maximum efficiency of BIPT systems with double-sided LCC compensation network is analyzed. To realize load matching and power flow regulation, an optimal dual side phase shift control strategy is proposed. Furthermore, a time domain model of double-sided LCC compensation network is proposed to describe the behavior of the BIPT systems, including the ZVS operation range. With the time domain analysis, it turns out the system has narrow ZVS operation range only in light duty and heavy duty with the proposed dual side phase shift control. So the third phase shift between primary and secondary full bridges is introduced as an additional control variable, which forms the TPS control. With the proposed TPS control, ZVS of all switches in both primary and secondary sides over entire power range can be achieved. A prototype of 1kW BIPT system was built to verify the theoretical analysis. Experimental waveforms were in good agreement with the proposed time domain model, and all power switched realized ZVS over entire power range and wide coupling coefficient in different DC bus voltage ratio. A peak system efficiency of 94.83% was measured with an output power of 1021W.

References

[1] J. Yungtaek and M. M. Jovanovic, "A contactless electrical energy transmission system for portable-telephone battery chargers," *IEEE Trans. Ind. Electron.*, vol. 50, no. 3, pp. 520-527, June 2003.

[2] S. Y. R. Hui and W. W. C. Ho, "A New Generation of Universal Contactless Battery Charging Platform for Portable Consumer Electronic Equipment," *IEEE Trans. Power Electron.*, vol. 20, no. 3, pp. 620-627, May 2005.

[3] S. Ping, A. P. Hu, S. Malpas, and D. Budgett, "A frequency control method for regulating wireless power to implantable devices," *IEEE Trans Biomed Circuits Syst,* vol. 2, no. 1, pp. 22-9, Mar 2008.

[4] C. Qianhong, W. Siu Chung, C. K. Tse, and R. Xinbo, "Analysis, design, and control of a transcutaneous power regulator for artificial hearts," *IEEE Trans Biomed Circuits Syst,* vol. 3, no. 1, pp. 23-31, Feb 2009.

[5] T. Assaf, C. Stefanini, and P. Dario, "Autonomous Underwater Biorobots: A Wireless System for Power Transfer," *IEEE Robotics & Automation Magazine,* vol. 20, no. 3, pp. 26-32, 2013.

[6] T. Kan, R. Mai, P. P. Mercier, and C. Mi, "Design and Analysis of a Three-Phase Wireless Charging System for Lightweight Autonomous Underwater Vehicles," *IEEE Trans. Power Electron.,* pp. 1-1, 2017.

[7] G. A. Covic and J. T. Boys, "Modern Trends in Inductive Power Transfer for Transportation Applications," *IEEE Trans. Emerg. Sel. Topics Power Electron.,* vol. 1, no. 1, pp. 28-41, 2013.

[8] R. Bosshard and J. W. Kolar, "All-SiC 9.5 kW/dm^3 On-Board Power Electronics for 50 kW/85 kHz Automotive IPT System," *IEEE Trans. Emerg. Sel. Topics Power Electron.,* vol. 5, no. 1, pp. 419-431, 2017.

[9] Y. Guo, L. Wang, Q. Zhu, C. Liao, and F. Li, "Switch-On Modeling and Analysis of Dynamic Wireless Charging System Used for Electric Vehicles," *IEEE Trans. Ind. Electron.,* vol. 63, no. 10, pp. 6568-6579, 2016.

[10] J. M. Miller and A. Daga, "Elements of Wireless Power Transfer Essential to High Power Charging of Heavy Duty Vehicles," *IEEE Trans. Transport. Electrific.,* vol. 1, no. 1, pp. 26-39, 2015.

[11] H. Feng, T. Cai, S. Duan, J. Zhao, X. Zhang, and C. Chen, "An LCC-Compensated Resonant Converter Optimized for Robust Reaction to Large Coupling Variation in Dynamic Wireless Power Transfer," *IEEE Trans. Ind. Electron.,* vol. 63, no. 10, pp. 6591-6601, 2016.

[12] J. H. Kim *et al.*, "Development of 1-MW Inductive Power Transfer System for a High-Speed Train," *IEEE Trans. Ind. Electron.,* vol. 62, no. 10, pp. 6242-6250, 2015.

[13] G. A. Covic and J. T. Boys, "Inductive Power Transfer," *Proceedings of the IEEE,* vol. 101, no. 6, pp. 1276-1289, 2013.

[14] C. Park, S. Lee, S. Y. Jeong, G.-H. Cho, and C. T. Rim, "Uniform Power I-Type Inductive Power Transfer System With *DQ*-Power Supply Rails for On-Line Electric Vehicles," *IEEE Trans. Power Electron.,* vol. 30, no. 11, pp. 6446-6455, 2015.

[15] R. Tavakoli and Z. Pantic, "Analysis, Design and Demonstration of a 25-kW Dynamic Wireless Charging System for Roadway Electric Vehicles," *IEEE Trans. Emerg. Sel. Topics Power Electron.,* pp. 1-1, 2017.

[16] C. Carretero, "Coupling Power Losses in Inductive Power Transfer Systems With Litz-Wire Coils," *IEEE Trans. Ind. Electron.,* vol. 64, no. 6, pp. 4474-4482, 2017.

[17] J. Sallan, J. L. Villa, A. Llombart, and J. F. Sanz, "Optimal Design of ICPT Systems Applied to Electric Vehicle Battery Charge," *IEEE Trans. Ind. Electron.,* vol. 56, no. 6, pp. 2140-2149, 2009.

[18] J. zhao, T. Cai, S. Duan, H. Feng, C. Chen, and X. Zhang, "A General Design Method of Primary Compensation Network for Dynamic WPT System Maintaining Stable Transmission Power," *IEEE Trans. Power Electron.,* pp. 1-1, 2016.

[19] X. Dai, X. Li, Y. Li, and A. P. Hu, "Impedance-Matching Range Extension Method for Maximum Power Transfer Tracking in IPT System," *IEEE Trans. Power Electron.,* vol. 33, no. 5, pp. 4419-4428, 2018.

[20] U. K. Madawala and D. J. Thrimawithana, "A Bidirectional Inductive Power Interface for Electric Vehicles in V2G Systems," *IEEE Trans. Ind. Electron.,* vol. 58, no. 10, pp. 4789-4796, 2011.

[21] D. J. Thrimawithana and U. K. Madawala, "A Generalized Steady-State Model for Bidirectional IPT Systems," *IEEE Trans. Power Electron.,* vol. 28, no. 10, pp. 4681-4689, 2013.

[22] A. K. Swain, M. J. Neath, U. K. Madawala, and D. J. Thrimawithana, "A Dynamic Multivariable State-Space Model for Bidirectional Inductive Power Transfer Systems," *IEEE Trans. Power Electron.,* vol. 27, no. 11, pp. 4772-4780, 2012.

[23] A. A. S. Mohamed, A. Berzoy, and O. A. Mohammed, "Experimental Validation of Comprehensive Steady-State Analytical Model of Bidirectional WPT System in EVs Applications," *IEEE Trans. Veh. Technol,* vol. 66, no. 7, pp. 5584-5594, 2017.

[24] Y. Tang, Y. Chen, U. K. Madawala, D. J. Thrimawithana, and H. Ma, "A New Controller for Bi-directional Wireless Power Transfer Systems," *IEEE Trans. Power Electron.,* vol. PP, no. 99, pp. 1-1, 2017.

[25] R. Bosshard, J. W. Kolar, and B. Wunsch, "Control method for Inductive Power Transfer with high partial-load efficiency and resonance tracking," in *2014 International Power Electronics Conference (IPEC-Hiroshima 2014 - ECCE ASIA)*, Hiroshima, 2014, pp. 2167-2174.

[26] H. H. Wu, A. Gilchrist, K. D. Sealy, and D. Bronson, "A High Efficiency 5 kW Inductive Charger for EVs Using Dual Side Control," *IEEE Trans. Ind. Informat.,* vol. 8, no. 3, pp. 585-595, 2012.

[27] T. Diekhans and R. W. De Doncker, "A Dual-Side Controlled Inductive Power Transfer System Optimized for Large Coupling Factor Variations and Partial Load," *IEEE Trans. Power Electron.,* vol. 30, no. 11, pp. 6320-6328, 2015.

[28] R. Mai, Y. Liu, Y. Li, P. Yue, G. Cao, and Z. He, "An Active-Rectifier-Based Maximum Efficiency Tracking Method Using an Additional Measurement Coil for Wireless Power Transfer," *IEEE Trans. Power Electron.,* vol. 33, no. 1, pp. 716-728, 2018.

[29] K. Colak, E. Asa, M. Bojarski, D. Czarkowski, and O. C. Onar, "A Novel Phase-Shift Control of Semibridgeless Active Rectifier for Wireless Power Transfer," *IEEE Trans. Power Electron.,* vol. 30, no. 11, pp. 6288-6297, 2015.

[30] B. X. Nguyen *et al.*, "An Efficiency Optimization Scheme for Bidirectional Inductive Power Transfer Systems," *IEEE Trans. Power Electron.,* vol. 30, no. 11, pp. 6310-6319, 2015.

[31] S. Li, W. Li, J. Deng, T. D. Nguyen, and C. C. Mi, "A Double-Sided LCC Compensation Network and Its Tuning Method for Wireless Power Transfer," *IEEE Trans. Veh. Technol,* vol. 64, no. 6, pp. 2261-2273, 2015.

[32] D. J. Thrimawithana, U. K. Madawala, and M. Neath, "A Synchronization Technique for Bidirectional IPT Systems," *IEEE Trans. Ind. Electron.,* vol. 60, no. 1, pp. 301-309, 2013.

Xiaoming Zhang received the B.S. degree in electrical engineering and automation from Huazhong University of Science and Technology, Wuhan, China, in 2014, where he is currently working toward the Ph.D. degree in the School of Electrical and Electronics Engineering.

His research interests include wireless power transmission and power electronics applied to electric vehicles.

Tao Cai received the Ph.D. degree in control science and engineering from Huazhong University of Science and Technology, Wuhan, China, in 2004.

He is currently with Huazhong University of Science and Technology. He has authored or coauthored about 20 technical papers published in journals and conference proceedings. His current research interests include advanced signal processing and energy management of renewable power generation.

Shanxu Duan (SM'16) received the B.S., M.S., and Ph.D. degrees in electrical engineering from Huazhong University of Science and Technology, Wuhan, China, in 1991, 1994, and 1999, respectively.

Since 1991, he has been a Faculty Member with the College of Electrical and Electronics Engineering, Huazhong University of Science and Technology, where he is currently a Professor. His research interests include stabilization, nonlinear control with application to power electronic circuits and systems, fully digitalized control techniques for power electronics apparatus and systems, and optimal control theory and corresponding application techniques for high-frequency pulse-width modulation power converters.

Dr. Duan is a Senior Member of the Chinese Society of Electrical Engineering and a Council Member of the Chinese Power Electronics Society. He was selected as one of the New Century Excellent Talents by the Ministry of Education of China in 2007. He was also the recipient of the honor of "Delta Scholar" in 2009.

This article has been accepted for publication in a future issue of this journal, but has not been fully edited. Content may change prior to final publication. Citation information: DOI 10.1109/TIE.2018.2871794, IEEE Transactions on Industrial Electronics

Hao Feng received the B.S. degree in control engineering and Ph.D. degrees in electrical engineering from Huazhong University of Science and Technology, Wuhan, China, in 2013 and 2018, respectively.

His research interests include inductive power transfer systems, resonant converters, renewable energy integration and large capacity energy storage system.

Hongsheng Hu received the B.S. degree in electrical engineering from Huazhong University of Science and Technology, Wuhan, China, in 2014, where he is currently working toward the Ph.D. degree in the School of Electrical and Electronics Engineering.

His research interests include wireless power transfer and magnetic design.

Jintao Niu received the B.S. degree in water conservancy and hydropower engineering from Huazhong University of Science and Technology, Wuhan, China, in 2016, where he is currently working toward the Master's degree in the School of Electrical and Electronics Engineering.

His research interests include high-power battery charger and energy management system.

Changsong Chen received the Ph.D. degree in electrical engineering from Huazhong University of Science and Technology, Wuhan, China, in 2011.

He was a Postdoctoral Research Fellow with the Department of Control Science and Engineering, Huazhong University of Science and Technology, from 2011 to 2013. He is currently a Faculty Member in the School of Electrical and Electronics Engineering, Huazhong University of Science and Technology. His current research interests include renewable energy applications, microgrids, and power electronics applied to electric vehicles.